

Assessment of Cellular Signals of Opportunity for High-Altitude Aircraft Navigation

Zaher (Zak) M. Kassas ^{ID}, The Ohio State University, Columbus, OH 43210 USA
Joe Khalife ^{ID} and **Ali Abdallah** ^{ID}, University of California, Irvine, Irvine, CA 92697 USA
Chiawei Lee ^{ID}, **Juan Jurado** ^{ID}, **Steven Wachtel**, **Jacob Duede**, **Zachary Hoeffner**,
Thomas Hulsey and **Rachel Quirarte**, U.S. Air Force, Edwards, CA 93524 USA
RunXuan Tay, Republic of Singapore Air Force, Singapore

INTRODUCTION

Modern aircraft navigation systems are highly dependent on global navigation satellite system (GNSS) signals and their augmentation systems (e.g., ground-based augmentation system and space-based augmentation system). GNSS provides the aircraft with an accurate and reliable position, speed, and time estimate at any point and without interruption. GNSS is also relied on in aviation communications, navigation, and surveillance systems as well as air traffic management [1].

Over the past few years, GNSS radio frequency interference (RFI) incidents skyrocketed, jeopardizing safe and efficient aviation operations. RFI sources include repeaters and pseudolites, GNSS jammers, and systems transmitting outside the GNSS frequency bands [2]. According to EUROCONTROL, a pan-European, civil-military organization dedicated to supporting European aviation, there were 4364 GNSS outages reported by pilots in 2018, which represents more than a 2000% increase over the previous year [3]. What is alarming is that while the majority of RFI hotspots appear related to conflict zones, they affect civil aviation at distances of up to 300 km from these zones. What is also alarming is that the

majority of RFI (about 81%) affects en-route flights, even though this is where RFI should be at its lowest, as the aircraft is as far away from a ground-based interferer as possible. In 2019, the International Civil Aviation Organization issued a Working Paper titled “An Urgent Need to Address Harmful Interferences to GNSS,” where it concluded that harmful RFI to GNSS would prevent the full continuation of safety and efficiency benefits of GNSS-based services. Moreover, there was a call for supporting the multidisciplinary development of alternative positioning, navigation, and timing (PNT) strategy and solutions to complement the use of GNSS in aviation [4].

In 2021, the U.S. Department of Transportation released the “Complementary Positioning, Navigation, and Timing (PNT) and GPS Backup Technologies Demonstration Report” to the U.S. Congress. The report concluded that while there are suitable, mature, and commercially available technologies to back up or to complement GPS, none of these systems alone can universally back up the PNT capabilities provided by GPS and its augmentations, necessitating a diverse universe of PNT technologies [5]. Moreover, in 2021, the National Institute of Standards and Technology issued a report on “Foundational PNT Profile: Applying the Cybersecurity Framework for the Responsible Use of PNT Services,” where it identified signals of opportunity (SOPs) and terrestrial RF sources (e.g., cellular) as a mitigation category that apply to the PNT profile [6]. Indeed, SOPs [7], particularly from cellular infrastructure [8]–[13], have shown tremendous promise over the past decade as an alternative PNT source [14]. This is due to their inherently desirable attributes for navigation purposes as follows:

- i) they are ubiquitous;
- ii) they are transmitted in a wide range of frequencies and in many directions, which makes them spectrally and geometrically diverse;

Authors' current addresses: Zaher (Zak) M. Kassas, The Ohio State University, Columbus, OH 43210 USA (e-mail: zkassas@ieee.org); Joe Khalife and Ali Abdallah, University of California, Irvine, Irvine, CA 92697 USA; Chiawei Lee, Juan Jurado, Steven Wachtel, Jacob Duede, Zachary Hoeffner, Thomas Hulsey, and Rachel Quirarte U.S. Air Force, Edwards, CA 93524 USA; RunXuan Tay, Republic of Singapore Air Force, Singapore. (Corresponding author: Zaher M. Kassas).

Manuscript received 28 June 2021, revised 13 January 2022; accepted 1 June 2022, and ready for publication 29 June 2022.

Review handled by Erik Blasch.
 0885-8985/22/\$26.00 © 2022 IEEE

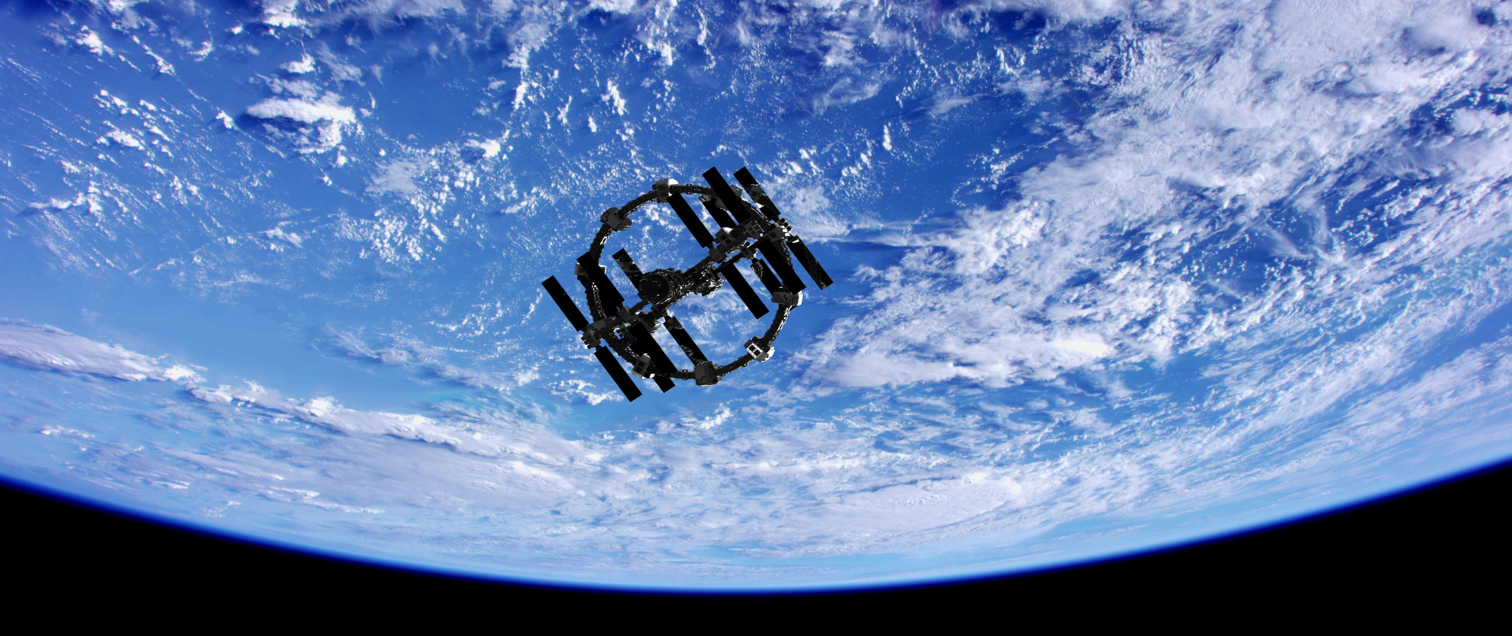


Image licensed by Ingram Publishing

- iii) they possess a high received carrier-to-noise (CNR) ratio (tens of dBs higher than GPS); and
- iv) they are readily available for free as their infrastructure is well established and the signals are broadcasted to billions of users worldwide.

Recent results have shown the ability of cellular SOPs to yield meter-level-accurate navigation on ground vehicles [15]–[18] in urban environments and submeter-level-accurate navigation on UAVs [19], [20]. Moreover, the robustness and availability of cellular SOPs have been demonstrated in a GPS-jammed environment [21].

Assessing cellular signals for aerial vehicles has been the subject of several studies recently [22], [23]. These studies span radio channel modeling [24]–[26]; evaluation of signal quality in terms of received signal power [27], [28], interference from cellular transmitters [29]–[31], and coverage and connectivity [32], [33]; and standards recommendations [34], [35]. According to existing studies, commercial cellular networks are capable of providing connectivity to aerial vehicles at low altitudes. However, the majority of published studies focused on evaluating cellular signals for communication purposes with little attention to evaluating them for navigation purposes [36]. Moreover, these studies only considered i) UAVs flying at low altitudes (up to 500 ft) and ii) slow speeds (up to 50 km/h). As such, existing studies are insufficient to reveal the potential and challenges associated with aviation operations. On the one hand, there is a lack of understanding of cellular signal attenuation and interference issues when received by aircraft flying at higher altitudes. On the other hand, there is a lack of assessment of the Doppler effect on tracking cellular synchronization signals for aircraft traveling at high speeds. Consider, for example, a Piper PA-18, a Boeing 747, and an F22 Raptor, which could reach speeds of 200, 1000, and 2400 km/h, respectively,

yielding Doppler frequency shifts at cellular frequencies of few hundred to several thousand Hz [37]. This study aims to perform the first assessment of cellular SOPs for high-altitude aircraft navigation by addressing the following questions:

- 1) Can cellular SOPs be received and exploited properly at aircraft altitudes and speeds to produce a robust navigation solution?
- 2) Does the downward tilt of cellular base station antennas prohibit reliable reception at high altitudes?
- 3) Is there a sufficient number of hearable cellular base stations to produce a navigation solution over long trajectories for high-altitude aircraft?

To answer these questions, an unprecedented aerial campaign was conducted in March 2020 by the Autonomous Systems Perception, Intelligence, and Navigation (ASPIN) Laboratory in collaboration with the United States Air Force (USAF) at the Edwards Air Force Base (AFB), California, USA. The cellular software-defined radios (SDRs) of the ASPIN Laboratory were flown on a USAF Beechcraft C-12 Huron, a fixed-wing aircraft, to collect ambient cellular 3G code-division multiple access (CDMA) and 4G long-term evolution (LTE) signals over Southern California. This unique dataset consists of combinations of flight run over three different environments (rural, semiurban, and urban) with altitudes ranging up to 23,000 ft and a multitude of trajectories and maneuvers including straight segments, banking turns, holding patterns, and ascending and descending teardrops, performed by members of the USAF Test Pilot School. This article assesses the collected signals for navigation purposes, with the aim to show that should GNSS signals become unavailable or unreliable midflight, cellular SOPs could be used to produce a sustainable and accurate navigation solution. In particular, this article characterizes the CNR as a function of altitude and horizontal distance.



Figure 1.
USAF Pilots and ASPIN researchers with the C-12 aircraft.

The CNR influences the precision of the navigation observables produced by a navigation receiver. It is found that up to a dozen base stations can be acquired and tracked at 23,000 ft above ground level (AGL). Furthermore, the multipath channel is analyzed at different altitudes in different regions. Multipath can cause significant biases in navigation observables, compromising the accuracy of the navigation solution. Ground reflections could be a concern for strong multipath. However, the data shows clean channels between the aircraft and the cellular base stations with a dominantly strong line-of-sight (LOS) component at all altitudes, which in turn means that the navigation observables from cellular SOPs will have high accuracy. To demonstrate the feasibility of aircraft navigation with cellular SOPs, a sample trajectory of the C-12 aircraft was estimated using cellular SOPs only, yielding a three-dimensional (3D) 10.5 m position root-mean-squared error (RMSE) over a 51-km trajectory traversed over a period of 9 minutes at approximately 5000 ft AGL.

The rest of this article is organized as follows. The “Experimental Setup and Flight Regions” section describes the hardware and software setup with which the aircraft was equipped and overviews the environments in which the flight campaigns took place. The “Ground-to-Air Channel Characterization” section studies the i) downlink cellular channel (ground-to-air) in terms of received CNR at different aircraft altitudes, aircraft-to-transmitter range, and in different regions and ii) multipath effects in terms of the channel impulse response (CIR). The “Aircraft Navigation With Cellular Signals” section presents experimental aircraft navigation results exclusively with cellular signals. The “Conclusion” section summarizes the main findings of this article.

EXPERIMENTAL SETUP AND FLIGHT REGIONS

This section overviews the hardware and software setup used for data collection and processing. It also describes the flight regions and aircraft maneuvers.

HARDWARE AND SOFTWARE SETUP

For this study, the C-12 aircraft, called Ms. Mabel, was equipped with the following.

- A quad-channel universal software radio peripheral (USRP)-2955.
- Three consumer-grade 800/1900-MHz Laird cellular antennas.
- A peripheral component interconnect express cable.
- A desktop computer equipped with a solid-state drive for data storage.
- A laptop computer running the ASPIN Laboratory’s SDR, called MATRIX: Multichannel Adaptive TRansceiver Information eXtractor, for real-time monitoring of the signals, which was operated during the flight by a flight engineer to determine when, where, and what cellular signals were available to tune the USRP accordingly.
- A GPS antenna to i) feed GPS measurements for the aircraft navigation system and ii) discipline the USRP’s onboard GPS-disciplined oscillator.

Figure 1 shows the C-12 aircraft and the USAF pilots and ASPIN researchers (this article’s co-authors). The equipment was assembled at the ASPIN Laboratory on a special rack provided by the USAF and was shipped to be mounted on the C-12 aircraft. The three Laird antennas were connected to the USRP to capture impinging 3G and 4G signals, and the USRP was tuned to listen to three carrier frequencies corresponding to two 4G United States cellular providers and one 3G United States cellular provider, as shown in Figure 2. Terabytes of in-phase and quadrature samples were collected throughout the experiment with a sampling rate of 10 MSps per channel. The 3G and 4G cellular modules of the MATRIX SDR [38], [39] were then used to postprocess the stored samples to produce navigation observables: Doppler frequency, carrier phase, and pseudorange, along with

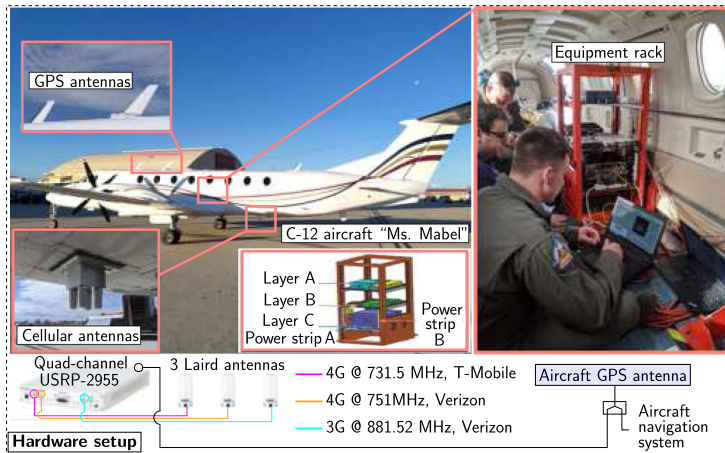


Figure 2. Hardware setup with which the C-12 aircraft was equipped.

corresponding CNRs. The hardware and software setup are shown in Figures 2 and 3, respectively.

FLIGHT REGIONS AND AIRCRAFT MANEUVERS

The campaign took place in three regions as follows.

- i) *Region A:* A rural region in Edwards AFB, California.
- ii) *Region B:* A semiurban region in Palmdale, California.
- iii) *Region C:* An urban region in Riverside, California.

Different maneuvers were planned over the three regions to test several aspects of aircraft navigation with cellular SOPs. Figure 4 shows the regions in which the experiments were performed. More than 70 3G base transceiver stations (BTSs) and 4G eNodeBs were mapped throughout the experiment via the method described in [40]. The mapped towers were cross-checked via Google Earth and online databases and are shown in Figure 4. This article investigates the potential of cellular SOPs for navigation; therefore, mapping the SOPs will not be discussed. The different maneuvers performed by the aircraft are described next.

Two main types of maneuvers were performed in each region. The first was a teardrop-like pattern while climbing/

descending. The patterns have a focal point that is aligned with geographic points of interest (see Figure 4). The measurements used to characterize the CNR and multipath were taken exactly above the geographic point of interest to maintain the horizontal distance between the aircraft and the cellular base stations. The second was a grid-like pattern with many turns and straight segments. Such patterns were used as stress-test for the navigation receivers to assess their ability to track cellular synchronization signals in a robust and accurate fashion as well as navigation solution evaluation. The two types of maneuvers are shown in Figure 5.

GROUND-TO-AIR CHANNEL CHARACTERIZATION

This section characterizes the ground-to-air radio channel by analyzing the CNR and multipath at different altitudes and horizontal distances in Regions A, B, and C.

CNR RATIO CHARACTERIZATION

The CNR influences the precision of the pseudorange navigation observable. The pseudorange is obtained by correlating the received cellular signal with known replicas of

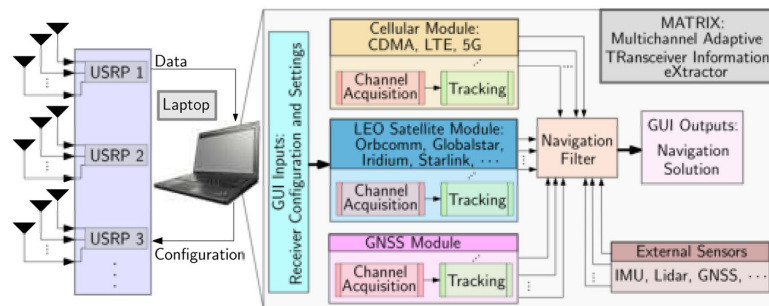
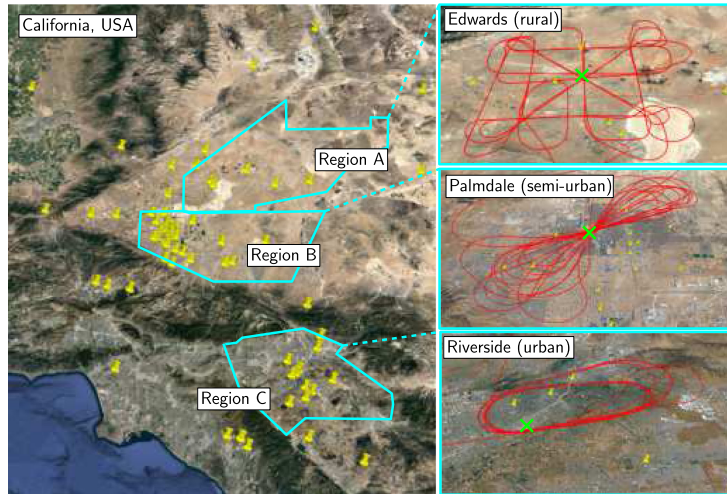
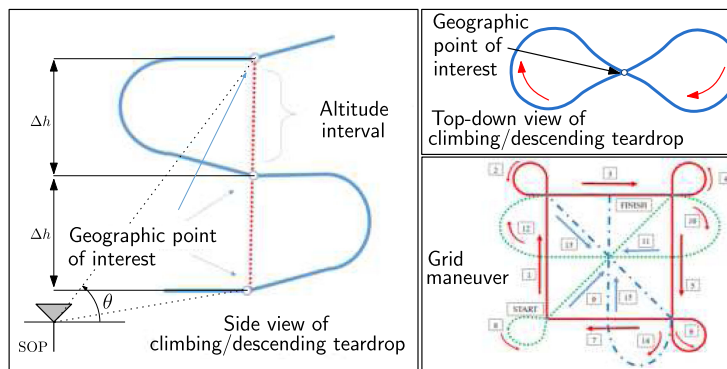


Figure 3. Software setup used for cellular SOP signal collection.


Figure 4.

Regions A, B, and C in which the flight campaigns took place. The yellow pins represent 3G and 4G cellular towers that were mapped and analyzed in this study. The right figures show the aircraft trajectory in all regions (shown in red). Geographic points of interest in each region, shown in green crosses, were chosen according to the designed trajectories.


Figure 5.

Maneuvers performed by the C-12 aircraft. The altitude step is denoted by Δh and θ denotes the elevation angle.

the synchronization sequences contained therein, such as the pseudorandom noise (PN) sequence in 3G CDMA and the primary synchronization signal and secondary synchronization signal in 4G LTE. The pseudorange observable is the delay of the autocorrelation peak, expressed in meters. The pseudorange is typically acquired through an exhaustive search over code phase shifts and Doppler frequencies then tracked with delay-locked loops (DLLs). Generally, the variance of the pseudorange error in a DLL is inversely proportional to the CNR. Roughly, the CNR must be above 20 dB-Hz for robust acquisition and tracking. High sensitivity receivers can acquire and track lower CNR signals, which is the subject of active research. The CNR can be calculated according to [41]

$$\text{CNR} = \frac{C}{N_0} = \frac{C}{\sigma_{\text{noise}}^2 T} \quad (1)$$

where C is the carrier power in Watts (W), N_0 is the noise power spectral density in W/Hz, which can be expressed as $N_0 = \sigma_{\text{noise}}^2 T$, where σ_{noise}^2 is the discretized noise variance and T is the accumulation period, or the period over which correlation in the DLL is performed. A cellular SOP receiver estimates σ_{noise}^2 by calculating the average power of the autocorrelation function of the received signal with a “fictitious” sequence that has similar properties as the transmitted sequences (e.g., a PN sequence that is not transmitted by any transmitter). The carrier power C is estimated by subtracting the noise variance from the peak power. The mapping between the CNR and the pseudorange error variance expressed in m^2 for a 3G cellular SOP receiver using a first-order DLL with a coherent discriminator is given by [38]

$$\sigma_{3G}^2 = c^2 \frac{B_{n,\text{DLL}} q(t_{\text{eml}})}{2(1 - 2B_{n,\text{DLL}} T) \text{CNR}} \quad (2)$$

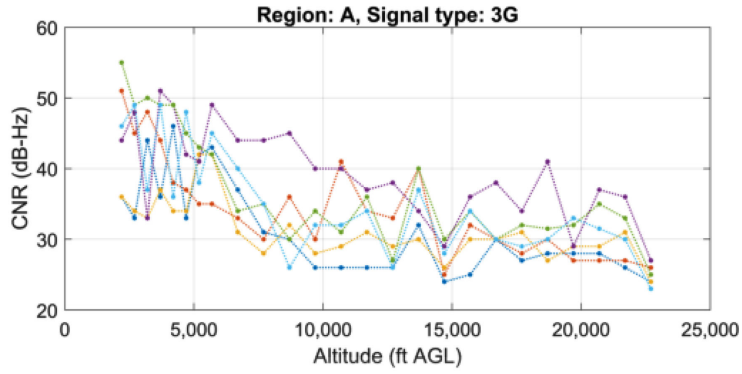


Figure 6. CNR of 6 3G BTSs as a function of altitude in Region A for 3G signals. Different lines corresponds to different cellular towers.

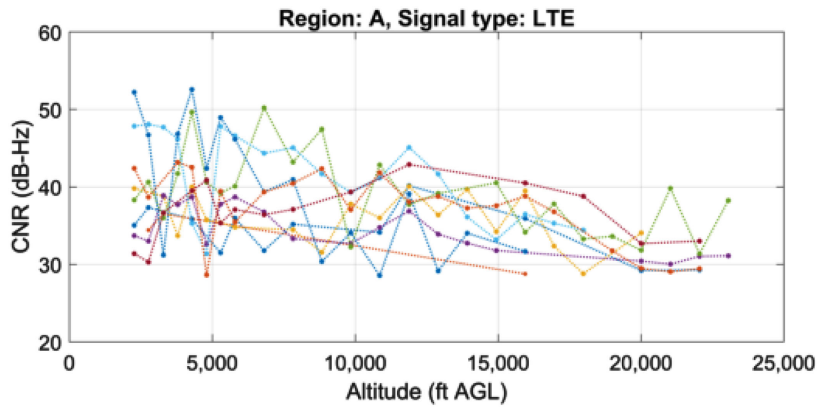


Figure 7. CNR of 9 LTE eNodeBs as a function of altitude in Region A for LTE signals. Different lines corresponds to different cellular towers.

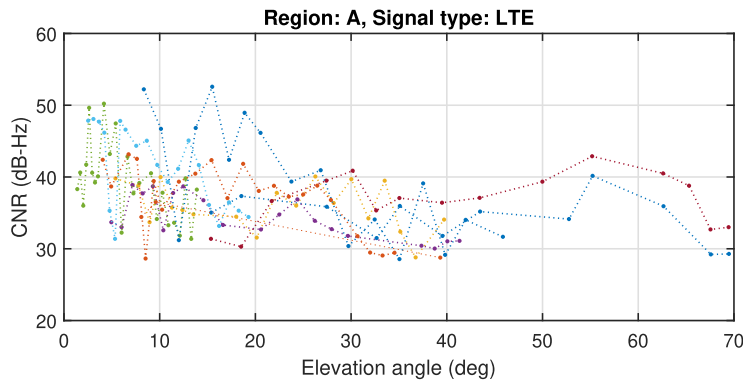


Figure 8. CNR of 9 LTE eNodeBs as a function of elevation in Region A for LTE signals. Different lines corresponds to different cellular towers

where c is the speed of light, $B_{n,DLL}$ is the DLL's noise equivalent bandwidth, and $q(t_{eml})$ is a sensitivity parameter that is a function of the autocorrelation function of the 3G cellular signal and the early minus-late time. For 4G LTE signals, this relationship becomes [39]

$$\sigma_{4G}^2 = c^2 \frac{\pi^2 T_s^2}{128 \lfloor \frac{N_r}{6} \rfloor \text{CNR}} \quad (3)$$

where T_s is the sample duration and N_r is the number of orthogonal frequency-division multiplexing subcarriers used in the synchronization sequence, and $\lfloor \cdot \rfloor$ is the floor

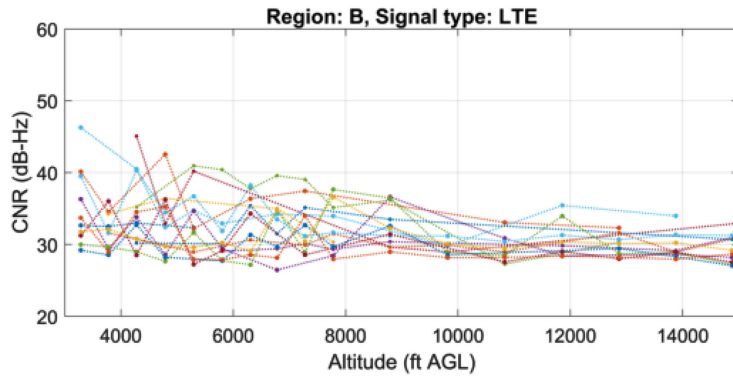


Figure 9.

CNR of 16 LTE eNodeBs as a function of altitude in Region B for LTE signals. Different lines corresponds to different cellular towers

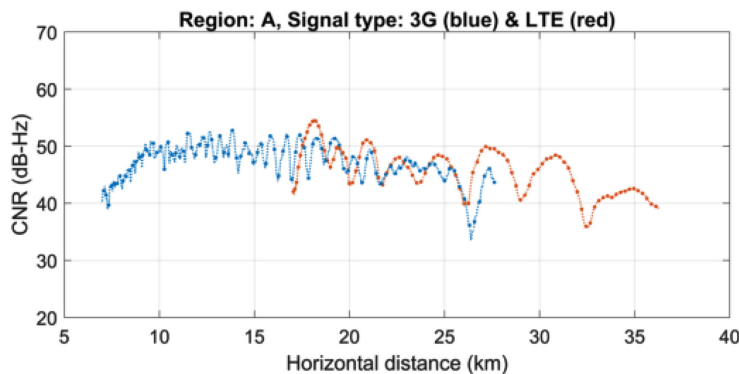


Figure 10.

CNR as a function of the horizontal distance for one 3G BTS (blue) and one LTE eNodeB (red). The aircraft was flying at about 5000 ft AGL.

function. It can be seen from (2) and (3) that the CNR is a crucial parameter in the precision of pseudorange measurements and must be characterized for aviation. In this experimental campaign, the CNRs were measured for i) a fixed horizontal distance and different altitudes and ii) a fixed altitude and different horizontal distances. The CNR as a function of altitude for Region A and both 3G and 4G signals are shown in Figures 6 and 7, respectively. Figure 8 shows the CNR as a function of elevation for 4G LTE signals in Region A. Figure 9 shows the CNR as a function of altitude for 4G LTE signals in Region B.

Figures 6–9 reveal that a significant number of cellular SOPs (namely, 73.33%) can be reliably acquired and tracked at altitudes up to 23,000 ft AGL. The reliable acquisition is qualified by the ability of detecting the presence of the signal along with producing a coarse estimate of the corresponding delays and Doppler shifts. Reliable tracking is qualified by maintaining bounded code and carrier phase errors. These bounded errors guarantee the reliability of the tracked signals to produce navigation observable(s) (pseudorange and carrier phase) which are used to produce a navigation solution. Typical path loss models would predict a linear decrease of the CNR as the distance increases. One

reason for seeing a sharp decrease over low altitudes is the directivity of cellular antennas in the elevation direction. It was observed that an elevation angle of about 20° seems to be a cutoff angle for the main lobe, above which the CNR decreases almost linearly with distance. However, the cellular SOP receivers were able to successfully track the signals all the way to 23,000 ft AGL, which corresponded to a maximum elevation angle of approximately 70° . This indicates that there is enough signal power in the side lobes to exploit for navigation purposes. The sharp decrease in CNR at low elevation angles also indicates that the cellular SOP navigation receiver would significantly benefit from a few degrees of an upward adjustment of cellular base station antennas. Although cellular providers require the downward tilt to minimize interference between different cells, the results shown in this article indicate that an upward adjustment is worth considering.

The CNRs for two base stations in Region A are plotted as a function of the horizontal distance in Figure 10. The curves in Figure 10 were expected to decrease as the horizontal distance increased. While this trend is visible, the CNRs also exhibit periodic behavior. This behavior could be due to the two-ray model, where ground

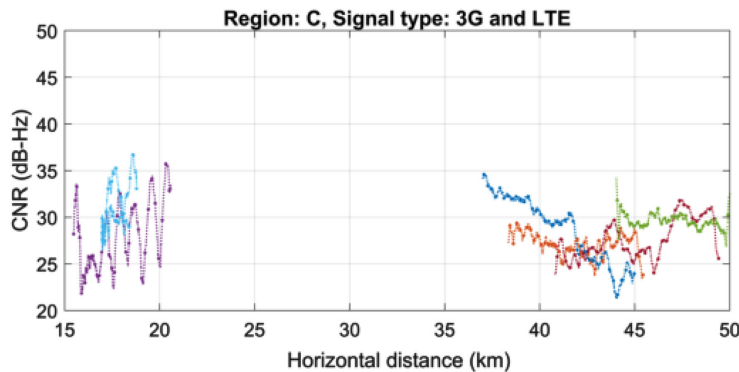


Figure 11.

CNR as a function of the horizontal distance for four 3G BTSs (blue, red, yellow, and purple) and two LTE eNodeBs (green and light blue). The aircraft was flying at an altitude of more than 16,000 ft AGL.

reflections cause constructive and destructive interference. This behavior was observed in reported results in the literature by other experimental campaigns [26].

The CNRs for six base stations in Region C are plotted as a function of the horizontal distance in Figure 11. It is worth noting that the aircraft was flying at an altitude of a little above 16,000 ft AGL, more than 11,000 ft higher than in Figure 11. At such altitudes, the elevation angles are very high. Since cellular base station antennas are tilted downward and are directional in the elevation direction, the loss due to the directive radiation pattern of cellular base station antennas dominates the path loss. This could explain why some of the CNRs in Figure 11 have an increasing trend, especially at shorter horizontal distances where the change in elevation angle is more significant. It is worth mentioning that the big hole in Figure 11 is purely due to this flight scenario, where the cellular base stations happened to be located either too close or too far with respect to the trajectory traversed by the aircraft.

MULTIPATH CHARACTERIZATION

The abovementioned study characterized the precision of pseudorange measurements via the CNR. Next, the accuracy of such measurements is characterized via the multipath channel. Severe- and short-delay multipath can introduce significant biases in the pseudorange measurement, which in turn degrades the navigation solution. One approach to characterize the multipath channel is by estimating the CIR. The cell-specific reference signal (CRS) in 4G LTE is transmitted for channel estimation purposes. The CIR is calculated at different altitudes in Regions A and B. Representative results for each region are shown in Figure 12. The bandwidth of the LTE signal used to estimate the CIRs was 10 MHz.

Figure 12 shows that the LOS signal dominates the CIR over altitudes up to 23,000 ft AGL. Figure 12 suggests that, as expected, multipath is most prominent at low

altitudes. This is due to the fact that less reflective surfaces are standing between the transmitter and the receiver. This can be seen as the CIRs are predominantly multipath-free or are experiencing low multipath. This implies high accuracy in the pseudorange measurements. Note that the CIRs seem to slightly degrade at altitudes of around 15,000 ft (AGL) and higher. That is due mostly to channel noise rather than multipath, as indicated in the CNR plots in Figures 6 and 7.

AIRCRAFT NAVIGATION WITH CELLULAR SIGNALS

The previous section established that cellular 3G and 4G SOPs are acquirable and trackable at altitudes as high as 23,000 ft AGL and that the channel possesses a dominant LOS component at the same range of altitudes. This section evaluates the navigation solution obtained exclusively with cellular SOP pseudoranges (without fusing any other sensors or signals, except for barometric altimeter measurements).

EXPERIMENT LAYOUT

The test trajectory consisted of a 1-2-3 leg from the grid pattern in Figure 4. Specifically, Leg 1 is a 24-km straight segment, followed by Leg 2, which is a 270° banking turn of length 18 km, and Leg 3 is a 9-km straight segment. The total distance traveled by the aircraft was over 51 km completed in 9 minutes. The aircraft's trajectory is shown in Figure 13. The aircraft maintained an altitude of approximately 5000 ft AGL over the trajectory. Three radio frequency channels were sampled as follows:

- i) 881.52 MHz, which is a 3G channel allocated for cellular provider Verizon Wireless;
- ii) 731.5 MHz, a 4G LTE channel allocated for AT&T; and

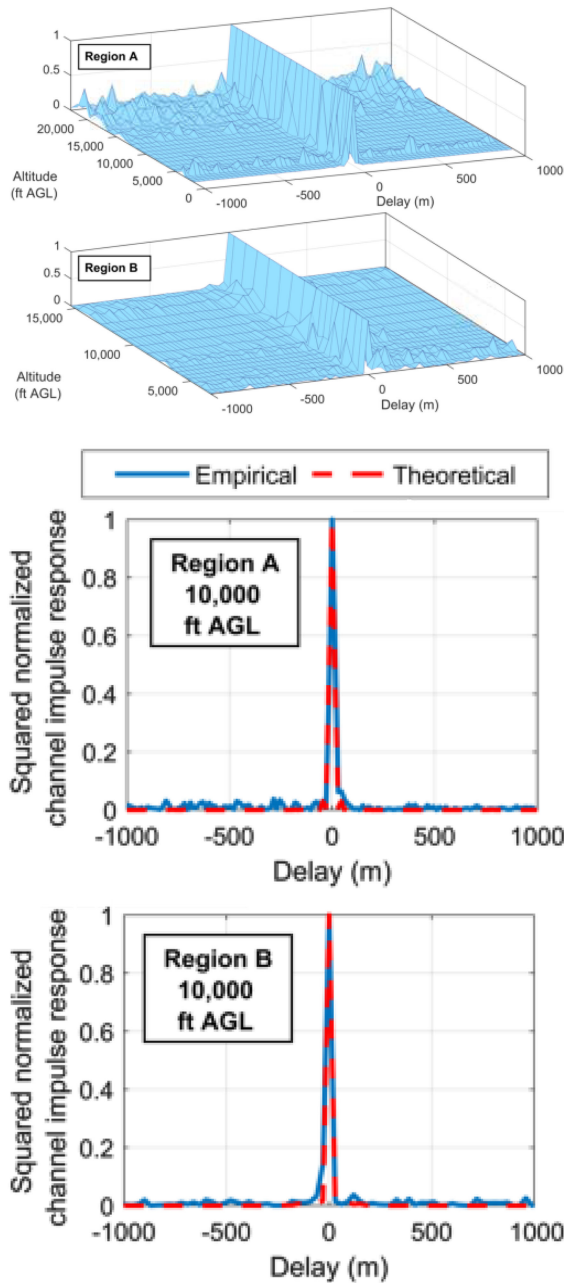


Figure 12.

Top: Surface plots of the CIR as a function of altitude for representative eNodeBs in Regions A and B. Bottom: Snapshots of empirical CIR in Regions A and B at 10,000 ft AGL along with the theoretical CIR.

- iii) 751 MHz, also a 4 G LTE channel allocated for T-Mobile.

A total of 11 cellular SOPs were heard over the three channels during the experiment as follows:

- a) six 3G BTSs; and
- b) five 4G eNodeBs.

TRACKING RESULTS

The 11 cellular SOPs were acquired at different times and tracked for different durations based on signal quality. The pseudorange to the n th base station can be modeled as [14]

$$z_n(k) = \|\mathbf{r}_r(k) - \mathbf{r}_{s_n}\|_2 + c\delta t_n(k) + v_n(k) \quad (4)$$

where \mathbf{r}_{s_n} is the n th base station's 3D position, c is the speed of light, $\{\delta t_n(k)\}_{n=1}^N$ is the difference between the aircraft-mounted receiver's and the n th cellular SOP's clock biases, with N being the total number of cellular SOPs, and $v_n(k)$ is the measurement noise, which is modeled as a zero-mean white sequence with variance $\sigma_n^2(k)$ obtained from the instantaneous CNR using the expression in (2) for 3G signals and the expression in (3) for 4G signals. Figures 14–16 show the time history of i) measured CNRs, ii) pseudorange measurements, and iii) pseudorange error (pseudorange minus the true range), for all 11 cellular SOPs, respectively. The true range is obtained from the known cellular SOPs' position and the aircraft's position throughout the entire flight, the latter of which was obtained from the aircraft's onboard navigation system.

The solid lines in Figure 15 depict the true range between the aircraft and the cellular SOPs, while the dashed lines show the receiver's pseudorange after removing the initial clock bias, i.e.

$$z'_n(k) = z_n(k) - c\hat{\delta}t_n(0)$$

where $\hat{\delta}t_n(0)$ is the initial clock bias estimate, obtained by differencing the true range between the aircraft and the cellular SOP position with the initial pseudorange measurement $z_n(0)$ produced by the receiver.

One can see from Figure 15 that pseudorange tracking is lost for some of the cellular SOPs at or around 300 s, which is when the aircraft starts banking to perform the 270° turn. It is suspected that the aircraft's wings and body block or severely attenuate some of the signals during banking, causing loss of tracking.

It is important to note that the average distance between the aircraft and the BTSs or eNodeBs was around 30 km over the entire trajectory, with eNodeB 4 being tracked at a 100-km distance in the first part of the trajectory. It is worth pointing that this study is a proof of concept to show the potential of exploiting cellular SOPs for aircraft navigation. The developed receiver is not a fully autonomous receiver and does not perform reacquisition of the same SOP after losing track. However, these signals were reacquirable (e.g., after banking).

NAVIGATION SOLUTION

Several estimators could be employed to estimate the aircraft's states (position, velocity, heading, and time) from

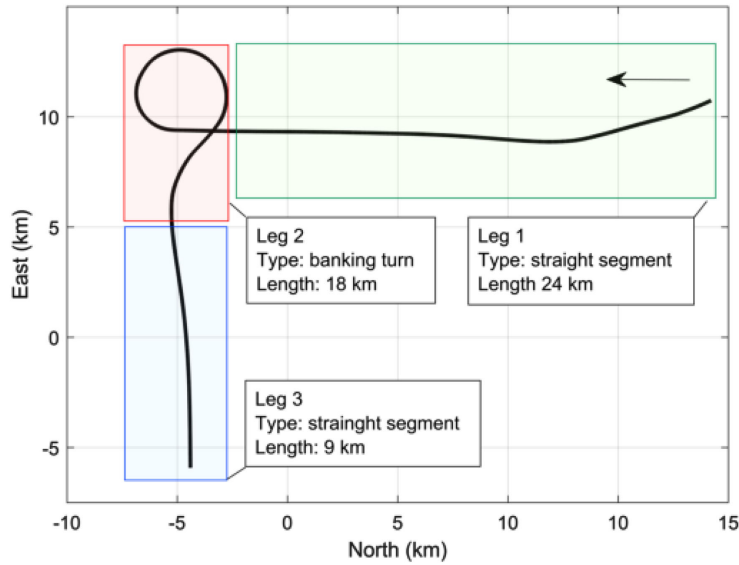


Figure 13. Aircraft trajectory for the aerial navigation experiment over Region A. The aircraft was flying at about 5000 ft AGL.

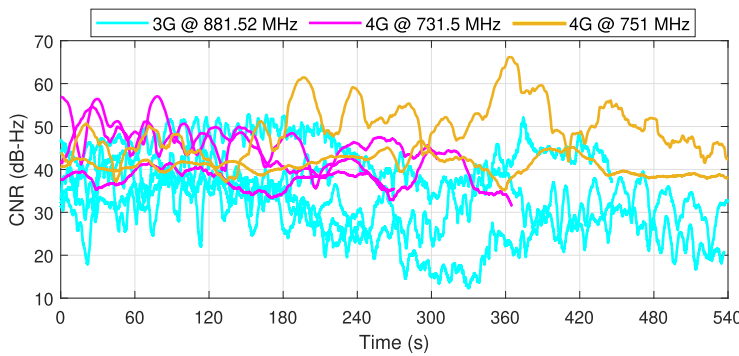


Figure 14. Time history of the CNRs for all the base stations used to compute the navigation solution.

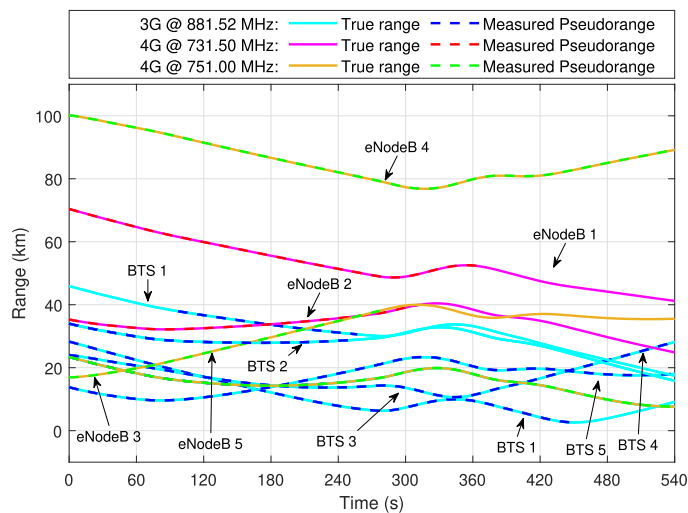
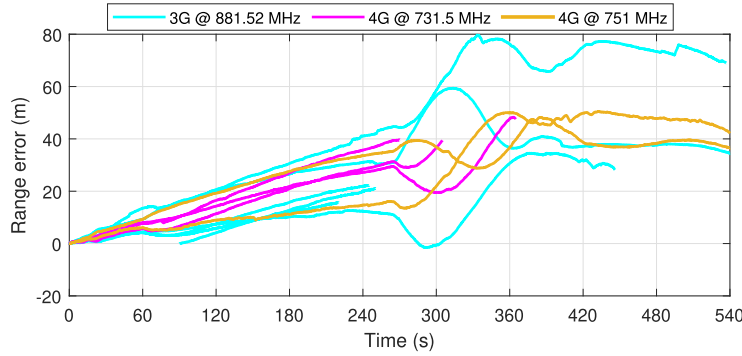


Figure 15. Time history of the pseudoranges estimated by the cellular SOP receivers and the corresponding true range. The initial values of the pseudoranges and ranges were subtracted out for ease of comparison.


Figure 16.

Time history of the pseudorange error (pseudorange minus the true range) for all cellular SOPs. The error is driven by a common term, which is the receiver's clock bias. The errors increase significantly at around 275 s, which is when the turn starts. The high dynamics of a banking turn inject stress on the tracking loops. The initial values of the pseudorange errors were subtracted out for ease of comparison.

pseudorange measurements. Moreover, data from other sensors [e.g., inertial measurement unit (IMU), radar, lidar, vision, etc.] and/or dynamical constraints could be fused with the pseudorange measurements to improve the navigation solution accuracy. However, the objective of this study is to test the potential of cellular SOPs to produce a navigation solution. Any additional sensors or dynamical constraints will only improve the performance of what is presented next. Since cellular SOPs suffer from low diversity in the vertical direction, only altitude measurements from the aircraft's navigation system were fused with the pseudorange measurements. The position of the cellular SOPs was assumed to be known, although it can be estimated on-the-fly as well [42]. However, the clock biases are dynamic and stochastic and must be estimated along with the aircraft's states. This results in an underdetermined system (i.e., one where the dimension of the state vector is larger than the dimension of the measurement vector), which makes using a point estimator (e.g., nonlinear least squares) infeasible [43]. To circumvent this, an extended Kalman filter (EKF) is used to produce the navigation solution with cellular pseudorange measurements and altimeter data derived from the aircraft's onboard navigation system. The aircraft's 3D position and velocity, denoted by \mathbf{r}_r and $\dot{\mathbf{r}}_r$, respectively, were estimated in a North–East–Down frame centered at the geographical point of interest of Region A. A simple, yet effective nearly constant velocity dynamical model was used to describe the dynamics of the aircraft, with power spectra given by q_N , q_E , and q_D for the acceleration process noise in the N , E , and D directions, respectively. A double integrator driven by process noise was used to model the receiver and base stations' clock biases [14]. The clock state of the receiver or any base station therefore consists of a time-varying, stochastic bias δt and drift $\delta \dot{t}$, with process noise power spectra $S_{\bar{w}_{\delta t}}$ and $S_{\bar{w}_{\delta \dot{t}}}$, respectively. The EKF was implemented using the framework described in [44]. To this end, define the state vector

$$\mathbf{x}(k) \triangleq [\mathbf{r}_r(k), \dot{\mathbf{r}}_r(k), c\delta t_1(k), \delta \dot{t}_1(k), \dots, c\delta t_N(k), \delta \dot{t}_N(k)]^T \in \mathbb{R}^{6+2N}. \quad (5)$$

The discrete-time dynamics of \mathbf{x} is given by

$$\mathbf{x}(k+1) = \mathbf{F}\mathbf{x}(k) + \mathbf{w}(k) \quad (6)$$

where $\mathbf{F} \triangleq \text{diag}[\mathbf{F}_{\text{pv}}, \mathbf{F}_{\text{clk}}, \dots, \mathbf{F}_{\text{clk}}]$

$$\mathbf{F}_{\text{pv}} \triangleq \begin{bmatrix} \mathbf{I}_{3 \times 3} & T\mathbf{I}_{3 \times 3} \\ \mathbf{0}_{3 \times 3} & \mathbf{I}_{3 \times 3} \end{bmatrix}, \quad \mathbf{F}_{\text{clk}} \triangleq \begin{bmatrix} 1 & T \\ 0 & 1 \end{bmatrix}$$

and T is the measurement update period, which is chosen to be the accumulation period in the receiver, and $\mathbf{w}(k)$ is the discrete-time process noise vector, which is modeled as a zero-mean white sequence with covariance $\mathbf{Q} \triangleq \text{diag}[\mathbf{Q}_{\text{pv}}, c^2\mathbf{Q}_{\text{clk}}]$

$$\mathbf{Q}_{\text{pv}} \triangleq \begin{bmatrix} \mathbf{S}_{\text{pv}} \frac{T^3}{3} & \mathbf{S}_{\text{pv}} \frac{T^2}{2} \\ \mathbf{S}_{\text{pv}} \frac{T^2}{2} & \mathbf{S}_{\text{pv}} T \end{bmatrix}, \quad \mathbf{S}_{\text{pv}} \triangleq \text{diag}[q_N, q_E, q_D]$$

$$\mathbf{Q}_{\text{clk}} = \mathbf{\Gamma} \mathbf{Q}_{\text{clk},r} \mathbf{\Gamma}^T + \mathbf{Q}_{\text{clk},\text{sop}}, \quad \mathbf{\Gamma} \triangleq [\mathbf{I}_{2 \times 2} \dots, \mathbf{I}_{2 \times 2}]^T$$

$$\mathbf{Q}_{\text{clk},\text{sop}} \triangleq \text{diag}[\mathbf{Q}_{\text{clk},\text{sop}_1}, \dots, \mathbf{Q}_{\text{clk},\text{sop}_N}]$$

$$\mathbf{Q}_{\text{clk},i} = \begin{bmatrix} S_{\bar{w}_{\delta t_i}} T + S_{\bar{w}_{\delta \dot{t}_i}} \frac{T^3}{3} & S_{\bar{w}_{\delta \dot{t}_i}} \frac{T^2}{2} \\ S_{\bar{w}_{\delta \dot{t}_i}} \frac{T^2}{2} & S_{\bar{w}_{\delta \dot{t}_i}} T \end{bmatrix}$$

where $i \in \{r, \text{sop}_1, \dots, \text{sop}_N\}$ and $S_{\bar{w}_{\delta t_i}}$ and $S_{\bar{w}_{\delta \dot{t}_i}}$ are the receiver or SOP-specific clock bias and drift noise power spectra.

The measurement (4) can be expressed in vector form as

$$z(k) = \mathbf{h}[\mathbf{x}(k)] + \mathbf{v}(k) \quad (7)$$

$$z(k) \triangleq [z_1(k), \dots, z_N(k), z_{\text{alt}}(k)]^T \in \mathbb{R}^{N+1}$$

$$\mathbf{v}(k) \triangleq [v_1(k), \dots, v_N(k), v_{\text{alt}}(k)]^T$$

where $\mathbf{h}[\mathbf{x}(k)]$ is a vector-valued function readily obtained from (4) and z_{alt} is the aircraft's altitude measurement. Let $\mathbf{R}(k)$ denote the covariance of the measurement noise vector $\mathbf{v}(k)$, which has the form $\mathbf{R}(k) =$

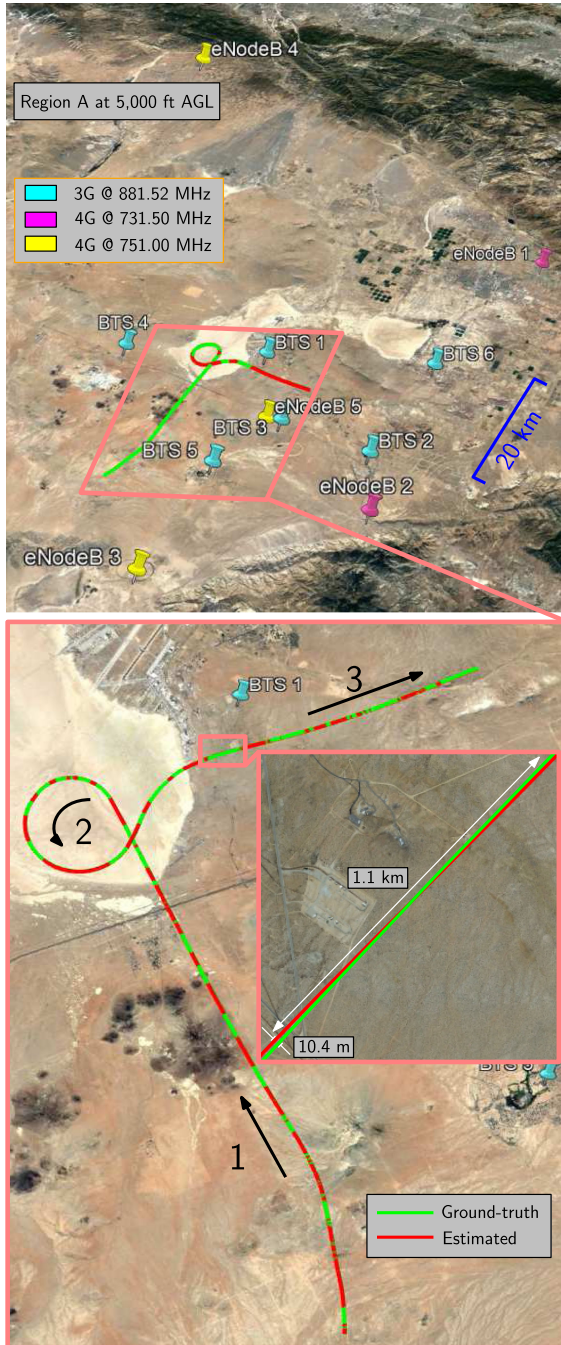


Figure 17.

Experimental layout and results showing: i) BTS and eNodeB positions, ii) true aircraft trajectory, and iii) aircraft trajectory estimated exclusively using cellular SOPs. The aircraft traversed a total distance of 51-km traversed in 9 minutes during the experiment. The 3D position RMSE over the entire trajectory was found to be 10.5 m.

$\text{diag}[\sigma_1^2, \dots, \sigma_N^2, \sigma_{\text{alt}}^2]$. The noise variances $\sigma_n^2(k)$ were obtained from the instantaneous CNR using the expression in (2) for 3G signals and the expression in (3) for 4G signals, while σ_{alt}^2 was set to 3 m^2 .

An EKF is then implemented based on the dynamics and measurement models in (6) and (7), respectively, to yield and

estimate $\hat{x}(k|k)$ of $x(k)$ using all measurements up to time-step k , with an associated estimation error covariance denoted by $\mathbf{P}(k|k)$. The initial estimate and covariance are obtained from two consecutive measurements and corresponding position estimates taken from the aircraft's navigation system [44]. The receiver and base station clock process noise covariance matrices were chosen to be

$$\mathbf{Q}_{\text{clk}_r} = \begin{bmatrix} 9.57 \times 10^{-5} & 2.52 \times 10^{-8} \\ 2.52 \times 10^{-8} & 1.89 \times 10^{-6} \end{bmatrix} \quad (8)$$

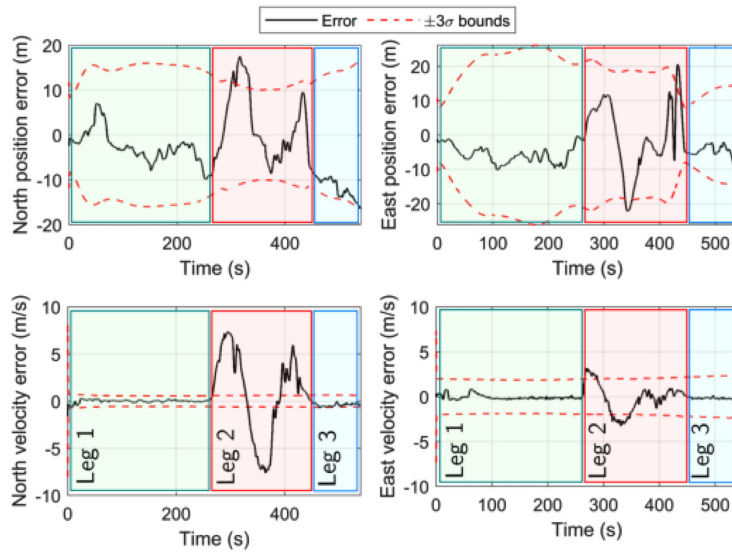
$$\mathbf{Q}_{\text{clk}_{,s_n}} = \begin{bmatrix} 3.11 \times 10^{-7} & 2.52 \times 10^{-11} \\ 2.52 \times 10^{-11} & 1.89 \times 10^{-9} \end{bmatrix}. \quad (9)$$

The abovementioned clock process noise covariance matrices assumed the receiver to be equipped with a typical-quality oven-controlled crystal oscillator (OCXO), while the cellular base stations are equipped with high-quality OCXOs [14]. The measurement rate was $T = 0.08/3 \text{ s}$. The power spectral densities of the acceleration in north and east directions were set to high values to account for not having an accurate dynamical model of the C-12 aircraft [45], specifically $q_N = q_E = 5 \text{ m}^2/\text{s}^3$. However, the power spectral density of the acceleration in the down direction was set to be small, since there was little change in altitude throughout the flight, specifically $q_D = 0.5 \text{ m}^2/\text{s}^3$.

Figure 17 shows the environment layout and the true and estimated trajectories. The total position 3D RMSE was calculated to be 10.5 m over the 51-km trajectory, traversed in 9 minutes. It is important to note that the position error in the EKF is the largest during the turn. This is due to i) the measurement errors due to the high dynamics of the banking turn, which severely stressed the tracking loops, and ii) the mismatch in the dynamics model assumed in the EKF since a 270° banking turn has significantly different dynamics than the assumed nearly constant velocity. However, as mentioned earlier, the purpose of this study is to highlight the minimum performance that can be achieved with SOPs. Any additional sensors, dynamical constraints, or adaptive estimators would improve the performance [46], [47]. Figure 18 shows the EKF estimation error plots and corresponding sigma-bounds for the aircraft's position and velocity states. The 3D navigation performance over the 51-km trajectory is summarized in Table 1.

DISCUSSION

This study showed the potential of cellular 3G and 4G SOPs as reliable sources for high-altitude aircraft navigation. The results presented herein, although promising, can be further improved upon in several ways. The following are key takeaways and design considerations for reliable aircraft navigation with cellular SOPs.


Figure 18.

EKF plots showing the time history of the position and velocity errors as well as the $\pm 3\sigma$ bounds. As expected, the EKF performs poorly in the second leg, where the mismatch between the true aircraft dynamics and the assumed EKF model is highest.

- *Long integration periods:* The period over which correlations were performed in the receiver could be extended to achieve higher CNRs where necessary, especially at altitudes above 23,000 ft. However, one would need a stable oscillator in the receiver clock to achieve coherent integration. As such, highly stable OCXOs or chip-scale atomic clocks could be used to drive the receiver's clock.
- *Mitigate self-blockage:* As discussed previously, the aircraft's body and wings caused signal blockage or severe attenuation during banking. One way to mitigate this is by mounting multiple antennas onto the aircraft in such a way that at least one antenna remains within LOS to the cellular base station of interest (e.g., at the tip of both wings). This guarantees continuous availability of pseudorange measurements. Another mitigation approach is to use synthetic aperture navigation (e.g., [48])
- *Accounting for the high dynamics:* Aircraft, such as the C-12, can perform highly dynamic maneuvers. As such, it is crucial to design tracking loops in the

receivers that can cope with such dynamics. Moreover, the dynamics model employed in the EKF in this study led to mismatches and larger estimation errors during the 270° turn. This mismatch can be mitigated by using appropriate dynamical models for fixed-wing aircraft or more elaborate dynamical models (e.g., Wiener process acceleration, Singer acceleration, mean-adaptive acceleration, semi-Markov jump process, circular motion, curvilinear motion, coordinated turn, among others [45]) adaptive estimation techniques [46], [47], and/or a kinematic model with IMU measurements, as is the case with most INS aiding techniques [16], [42].

- *Vertical dilution of precision:* At high altitudes, there is very little vertical diversity with respect to terrestrial cellular towers. As such, the aircraft's cellular-based navigation solution vertical dilution of precision will be large. Nevertheless, the aircraft's vertical position can still be estimated from the pseudoranges extracted from cellular towers, albeit with less accuracy compared to the results presented in this article, which fused altimeter-based measurements. For example, if the altimeter-based altitude measurements are not used in the demonstrated flight, a 2D and 3D RMSE of 30.41 and 117.55 m are achieved, respectively, compared to 10.53 and 10.55 m, respectively, when using altitude measurements.
- *Intrachannel interference:* The proposed receiver exploits the synchronization sequences or reference signals broadcast by cellular towers. These signals are designed to have low cross-correlation properties between different towers. For

Table 1.

Navigation Performance With Cellular Signals			
Metric	Leg 1	Leg 2	Leg 3
Position RMSE [m]	7.57	12.85	12.87
Velocity RMSE [m/s]	0.62	4.87	0.46
Maximum position error [m]	10.46	22.67	20.46
Maximum velocity error [m/s]	4.15	7.64	0.74

example, in 3G systems, a 32768-long QPSK pseudonoise (PN) sequence and Walsh codes are used to spread the transmitted data. The PN sequence is shifted by an integer multiple of 64 chips by each cellular tower sector, which allows a maximum of 512 possible shifts. In this case, the cross-correlation between the PN sequence and its shifted version is negligible. As such, for two towers to significantly interfere at the receiver, their relative range must be at least 15 km (corresponding to 64-chip offset). However, in practice, adjacent towers are offset by at least 4×64 chips, requiring a minimum of 60-km relative range for strong interference to occur. In addition, the 60-km relative range implies a 95 dB difference in the path loss (assuming the free space propagation model), which means that one signal will be completely buried in the noise floor of the other. Even for a relative range of 15 km, the difference in the path loss is 83 dB. In conclusion, it is very unlikely for intrachannel interference to be an impediment for exploiting 3G signals for aerial navigation. This could explain why interference from near and far cells have not been detected in the case of 3G signals. The same discussion holds for 4G signals, except that the synchronization signals were not used in the 4G module in order to avoid interference, since some of these sequences are common between different eNodeBs. Instead, only the CRS was used, which is unique for each eNodeB and has very low cross-correlation properties.

CONCLUSION

This study demonstrated that reliable acquisition and tracking of cellular 3G CDMA and 4G LTE signals can be performed by high dynamics aircraft flying at altitudes up to 23,000 ft AGL and horizontal distances up to 100 km, making them a reliable source for aircraft navigation. This finding is further validated by experimental results showing a USAF C-12 aircraft navigating for 51 km at around 5000 ft AGL over a 9-minute period exclusively with cellular SOPs, achieving a 3D position RMSE of 10.5 m.

ACKNOWLEDGMENTS

The authors would like to thank Edwards AFB and Holloman AFB for inviting the ASPIN Laboratory to conduct experiments on Air Force aircraft in the “SNIFFER: Signals of opportunity for Navigation In Frequency-Forbidden EnviRonments” flight campaign.

They would also like to thank Joshua Morales, Kimia Shamaei, Mahdi Maaref, Kyle Semelka, MyLinh Nguyen, and Trier Mortlock for their help with preparing for data collection. DISTRIBUTION STATEMENT A. Approved for public release; Distribution is unlimited 412TW-PA-20146. This work was supported in part by the Office of Naval Research (ONR) under Grant N00014-19-1-2511 and Grant N00014-19-1-2613, in part by the Sandia National Laboratories under Grant 1655264, in part by the National Science Foundation (NSF) under Grant 1929965, and in part by the U.S. Department of Transportation (USDOT) under Grant 69A3552047138 for the CARMEN University Transportation Center (UTC).

REFERENCES

- [1] R. Sabatini *et al.*, “Avionics systems panel research and innovation perspectives,” *IEEE Aerosp. Electron. Syst. Mag.*, vol. 37, no. 12, pp. 58–72, Dec. 2020.
- [2] E. Blasch *et al.*, “Cyber awareness trends in avionics,” in *Proc. IEEE/AIAA Digit. Avionics Syst. Conf.*, 2019, pp. 1–8.
- [3] EUROCONTROL, Aviation Intelligence Unit, “Does radio frequency interference to satellite navigation pose an increasing threat to network efficiency, cost-effectiveness and ultimately safety?,” Brussels, Belgium, Tech. Rep., Mar. 2021. [Online]. Available: <https://www.eurocontrol.int/sites/default/files/2021-03/eurocontrol-think-paper-9-radio-frequency-interference-satellite-navigation.pdf>
- [4] International Civil Aviation Organization (ICAO), “An urgent need to address harmful interferences to GNSS,” Montreal, QC, Canada, Tech. Rep., May 2019. [Online]. Available: <https://www.iata.org/contentassets/d7e421981aa64169af1a8d6b37438d4d/tib-gnss-interference-final.pdf>
- [5] A. Hansen *et al.*, “Complementary PNT and GPS backup technologies demonstration report: Sections 1 through 10,” Cambridge, MA, USA, John A. Volpe Nat. Transp. Syst. Center Tech. Rep. DOT-VNTSC-20-07, 2021.
- [6] M. Bartock *et al.*, “Foundational PNT profile: Applying the cybersecurity framework for the responsible use of positioning, navigation, and timing (PNT) services,” Gaithersburg, MD, USA, Nat. Inst. Standards and Technol. (NIST), Tech. Rep. NISTIR 8323, Feb. 2021.
- [7] J. Raquet *et al.*, “Part D: Position, navigation, and timing using radio signals-of-opportunity,” in *Position, Navigation, and Timing Technologies in the 21st Century: Integrated Satellite Navigation, Sensor Systems, and Civil Applications*, J. Morton, F. van Diggelen, J. Spilker, Jr., and B. Parkinson, Eds. Hoboken, NJ, USA: Wiley-IEEE, 2021, vol. 2, ch. 35–43, pp. 1115–1412.
- [8] J. del Peral-Rosado, R. Raulefs, J. López-Salcedo, and G. Seco-Granados, “Survey of cellular mobile radio localization methods: From 1G to 5G,” *IEEE Commun. Surv. Tut.*, vol. 20, no. 2, pp. 1124–1148, Apr.–Jun. 2018.

- [9] T. Kang, H. Lee, and J. Seo, "TOA-based ranging method using CRS in LTE signals," *J. Adv. Navigation Technol.*, vol. 23, no. 5, pp. 437–443, Oct. 2019.
- [10] P. Wang and Y. Morton, "Multipath estimating delay lock loop for LTE signal TOA estimation in indoor and urban environments," *IEEE Trans. Wireless Commun.*, vol. 19, no. 8, pp. 5518–5530, Aug. 2020.
- [11] J. Gante, L. Sousa, and G. Falcao, "Dethroning GPS: Low-power accurate 5G positioning systems using machine learning," *IEEE Trans. Emerg. Sel. Topics Circuits Syst.*, vol. 10, no. 2, pp. 240–252, Jun. 2020.
- [12] H. Dun, C. Tiberius, and G. Janssen, "Positioning in a multipath channel using OFDM signals with carrier phase tracking," *IEEE Access*, vol. 8, pp. 13011–13028, 2020.
- [13] A. Abdallah and Z. Kassas, "UAV navigation with 5G carrier phase measurements," in *Proc. ION GNSS Conf.*, 2021, pp. 3294–3306.
- [14] Z. Kassas, "Navigation with cellular signals of opportunity," in *Position, Navigation, and Timing Technologies in the 21st Century: Integrated Satellite Navigation, Sensor Systems, and Civil Applications*, J. Morton, F. van Diggelen, J. Spilker, Jr., and B. Parkinson, Eds. Hoboken, NJ, USA: Wiley-IEEE, vol. 2, ch. 38, 2021, pp. 1171–1223.
- [15] C. Yang, T. Nguyen, and E. Blasch, "Mobile positioning via fusion of mixed signals of opportunity," *IEEE Aerosp. Electron. Syst. Mag.*, vol. 29, no. 4, pp. 34–46, Apr. 2014.
- [16] Z. Kassas, M. Maaref, J. Morales, J. Khalife, and K. Shamaei, "Robust vehicular localization and map matching in urban environments through IMU, GNSS, and cellular signals," *IEEE Intell. Transp. Syst. Mag.*, vol. 12, no. 3, pp. 36–52, Jun. 2020.
- [17] J. del Peral-Rosado *et al.*, "Physical-layer abstraction for hybrid GNSS and 5G positioning evaluations," in *Proc. IEEE Veh. Technol. Conf.*, 2019, pp. 1–6.
- [18] M. Maaref and Z. Kassas, "Autonomous integrity monitoring for vehicular navigation with cellular signals of opportunity and an IMU," *IEEE Trans. Intell. Transp. Syst.*, vol. 23, no. 6, pp. 5586–5601, Jun. 2022.
- [19] K. Shamaei and Z. Kassas, "Sub-meter accurate UAV navigation and cycle slip detection with LTE carrier phase," in *Proc. 32nd Int. Tech. Meeting Satell. Division Inst. Navigation Conf.*, 2019, pp. 2469–2479.
- [20] J. Khalife and Z. Kassas, "On the achievability of sub-meter-accurate UAV navigation with cellular signals exploiting loose network synchronization," *IEEE Trans. Aerosp. Electron. Syst.*, early access, Mar. 31, 2022, doi: 10.1109/TAES.2022.3162770.
- [21] Z. Kassas, J. Khalife, A. Abdallah, and C. Lee, "I am not afraid of the GPS jammer: Resilient navigation via signals of opportunity in GPS-denied environments," *IEEE Aerosp. Electron. Syst. Mag.*, vol. 37, no. 7, pp. 4–19, Jul. 2022.
- [22] Qualcomm Technologies Inc., "LTE unmanned aircraft systems," San Diego, CA, USA, Tech. Rep. 1.0.1, May 2017. [Online]. Available: <https://www.qualcomm.com/documents/lte-unmanned-aircraft-systems-trial-report/>
- [23] Y. Zeng, Q. Wu, and R. Zhang, "Accessing from the sky: A tutorial on UAV communications for 5G and beyond," *Proc. IEEE*, vol. 107, no. 12, pp. 2327–2375, Dec. 2019.
- [24] R. Amorim, H. Nguyen, P. Mogensen, I. Kovacs, J. Wigard, and T. Sorensen, "Radio channel modeling for UAV communication over cellular networks," *IEEE Wireless Commun. Lett.*, vol. 6, no. 4, pp. 514–517, Aug. 2017.
- [25] X. Cai *et al.*, "An empirical air-to-ground channel model based on passive measurements in LTE," *IEEE Trans. Veh. Technol.*, vol. 68, no. 2, pp. 1140–1154, Feb. 2019.
- [26] W. Khawaja, I. Guvenc, D. Matolak, U. Fiebig, and N. Schneckenburger, "A survey of air-to-ground propagation channel modeling for unmanned aerial vehicles," *IEEE Commun. Surv. Tut.*, vol. 21, no. 3, pp. 2361–2391, Jul.–Sep. 2019.
- [27] K. Matheou *et al.*, "Analysis of at-altitude LTE power spectra for small unmanned aircraft system C2 communications," in *Proc. Integr. Commun., Navigation, Surveill. Conf.*, 2019, pp. 1–12.
- [28] X. Cai *et al.*, "Low altitude air-to-ground channel characterization in LTE network," in *Proc. Eur. Conf. Antennas Propag.*, 2019, pp. 1–5.
- [29] B. Van DerA. BerghChiumento, and S. Pollin, "LTE in the sky: Trading off propagation benefits with interference costs for aerial nodes," *IEEE Commun. Mag.*, vol. 54, no. 5, pp. 44–50, May 2016.
- [30] I. Kovacs, R. Amorim, H. Nguyen, J. Wigard, and P. Mogensen, "Interference analysis for UAV connectivity over LTE using aerial radio measurements," in *Proc. IEEE Veh. Technol. Conf.*, 2017, pp. 1–6.
- [31] R. J. Amorim, I. Wigard Kovacs, and T. Sorensen, "UAV Communications for 5G and Beyond," *Performance Enhancements for LTE-Connected UAVs: Experiments and Simulations*, Y. Zeng, I. R. Guvenc Zhang, G. Geraci, and D. Matolak, Eds. Hoboken, NJ, USA: Wiley-IEEE, 2021, ch. 5, pp. 139–161.
- [32] E. Teng, J. Diogo Falcao, and B. Iannucci, "Holes-in-the-sky: A field study on cellular-connected UAS," in *Proc. Int. Conf. Unmanned Aircr. Syst.*, 2017, pp. 1165–1174.
- [33] G. Athanasiadou, M. Batistatos, D. Zarbouti, and G. Tsoulos, "LTE ground-to-air field measurements in the context of flying relays," *IEEE Wireless Commun.*, vol. 26, no. 1, pp. 12–17, Feb. 2019.
- [34] A. Abdalla and V. Marojevic, "Communications standards for unmanned aircraft systems: The 3GPP perspective and research drivers," *IEEE Commun. Standards Mag.*, vol. 5, no. 1, pp. 70–77, Mar. 2021.
- [35] H. Maattanen, "UAV communications for 5G and beyond," *3GPP Standardization for Cellular-Supported UAVs*, Y. Zeng, I. Guvenc, R. Zhang, G. Geraci, and D. Matolak, Eds. Hoboken, NJ, USA: Wiley-IEEE, 2021, ch. 6, pp. 163–180.

- [36] E. Kim and Y. Shin, "Feasibility analysis of LTE-based UAS navigation in deep urban areas and DSRC augmentation," *Sensors*, vol. 19, no. 9, pp. 4192–4207, Apr. 2019.
- [37] B. Stevens and M. Younis, "Detection algorithm for cellular synchronization signals in airborne applications," *IEEE Access*, vol. 9, pp. 55555–55566, Apr. 2021.
- [38] J. Khalife, K. Shamaei, and Z. Kassas, "Navigation with cellular CDMA signals—Part I: Signal modeling and software-defined receiver design," *IEEE Trans. Signal Process.*, vol. 66, no. 8, pp. 2191–2203, Apr. 2018.
- [39] K. Shamaei and Z. Kassas, "LTE receiver design and multipath analysis for navigation in urban environments," *Navigation, J. Inst. Navigation*, vol. 65, no. 4, pp. 655–675, Dec. 2018.
- [40] J. Morales and Z. Kassas, "Optimal collaborative mapping of terrestrial transmitters: Receiver placement and performance characterization," *IEEE Trans. Aerosp. Electron. Syst.*, vol. 54, no. 2, pp. 992–1007, Apr. 2018.
- [41] P. Misra and P. Enge, *Global Positioning System: Signals, Measurements, and Performance*, 2nd ed. Lincoln, MA, USA: Ganga-Jamuna Press, 2010.
- [42] J. Morales and Z. Kassas, "Tightly-coupled inertial navigation system with signals of opportunity aiding," *IEEE Trans. Aerosp. Electron. Syst.*, vol. 57, no. 3, pp. 1930–1948, Jun. 2021.
- [43] Z. Kassas and T. Humphreys, "Receding horizon trajectory optimization in opportunistic navigation environments," *IEEE Trans. Aerosp. Electron. Syst.*, vol. 51, no. 2, pp. 866–877, Apr. 2015.
- [44] J. Khalife and Z. Kassas, "Opportunistic UAV navigation with carrier phase measurements from asynchronous cellular signals," *IEEE Trans. Aerosp. Electron. Syst.*, vol. 56, no. 4, pp. 3285–3301, Aug. 2020.
- [45] X. Li and V. Jilkov, "Survey of maneuvering target tracking. Part I: Dynamic models," *IEEE Trans. Aerosp. Electron. Syst.*, vol. 39, no. 4, pp. 1333–1364, Oct. 2003.
- [46] M. Yeddanapudi, Y. Bar-Shalom, and K. Pattipati, "IMM estimation for multitarget-multisensor air traffic surveillance," *Proc. IEEE*, vol. 85, no. 1, pp. 80–96, Jan. 1997.
- [47] J. Dunik, O. Kost, O. Straka, and E. Blasch, "Navigation and estimation improvement by environmental-driven noise mode detection," in *Proc. IEEE/ION Position, Location, Navigation Symp.*, 2020, pp. 925–932.
- [48] A. Abdallah and Z. Kassas, "Deep learning-aided spatial discrimination for multipath mitigation," in *Proc. IEEE/ION Position, Location, Navigation Symp.*, 2020, pp. 1324–1335.